Characterizing filaments in regions of high-mass star formation: High-resolution submilimeter imaging of the massive star-forming complex NGC 6334 with ArTéMiS[★]

Ph. André[1], V. Revéret[1], V. Könyves[1], D. Arzoumanian[1], J. Tigé[2], P. Gallais[1], H. Roussel[3], J. Le Pennec[1], L. Rodriguez[1], E. Doumayrou[1], D. Dubreuil[1], M. Lortholary[1], J. Martignac[1], M. Talvard[1], C. Delisle[1], F. Visticot[1], L. Dumaye[1], C. De Breuck[4], Y. Shimajiri[1], F. Motte[1], S. Bontemps[5], M. Hennemann[1], A. Zavagno[2], D. Russeil[2], N. Schneider[5, 6], P. Palmeirim[2, 1], N. Peretto[7], T. Hill[1], V. Minier[1], A. Roy[1], and K.L.J. Rygl[8]

(Affiliations can be found after the references)

ABSTRACT

Context. *Herschel* observations of nearby molecular clouds suggest that interstellar filaments and prestellar cores represent two fundamental steps in the star formation process. The observations support a picture of low-mass star formation according to which ∼ 0.1 pc-wide filaments form first in the cold interstellar medium, probably as a result of large-scale compression of interstellar matter by supersonic turbulent flows, and then prestellar cores arise from gravitational fragmentation of the densest filaments. Whether this scenario also applies to regions of high-mass star formation is an open question, in part because the resolution of *Herschel* is insufficient to resolve the inner width of filaments in the nearest regions of massive star formation.
Aims. In an effort to characterize the inner width of filaments in high-mass star forming regions, we imaged the central part of the NGC6334 complex at a factor of > 3 higher resolution than *Herschel* at 350 μm.
Methods. We used the large-format bolometer camera ArTéMiS on the APEX telescope and combined the high-resolution ArTéMiS data at 350 μm with *Herschel*/HOBYS data at 70–500 μm to ensure good sensitivity to a broad range of spatial scales. This allowed us to study the structure of the main narrow filament of the complex with a resolution of 8″ or < 0.07 pc at d ∼ 1.7 kpc.
Results. Our study confirms that this filament is a very dense, massive linear structure with a line mass ranging from ∼ 500 $M_\odot$/pc to ∼ 2000 $M_\odot$/pc over nearly 10 pc. It also demonstrates for the first time that its inner width remains as narrow as W ∼ 0.15 ± 0.05 pc all along the filament length, within a factor of < 2 of the characteristic 0.1 pc value found with *Herschel* for lower-mass filaments in the Gould Belt.
Conclusions. While it is not completely clear whether the NGC 6334 filament will form massive stars or not in the future, it is two to three orders of magnitude denser than the majority of filaments observed in Gould Belt clouds, and yet has a very similar inner width. This points to a common physical mechanism for setting the filament width and suggests that some important structural properties of nearby clouds also hold in high-mass star forming regions.

Key words. stars: formation – stars: circumstellar matter – ISM: clouds – ISM: structure – ISM: individual objects (NGC 6334) – submillimeter

1. Introduction

Understanding star formation is a fundamental issue in modern astrophysics (e.g., McKee & Ostriker 2007). Very significant observational progress has been made on this topic thanks to far-infrared and submillimeter imaging surveys with the *Herschel* Space Observatory. In particular, the results from the *Herschel* "Gould Belt" survey (HGBS) confirm the omnipresence of filaments in nearby clouds and suggest an intimate connection between the filamentary structure of the interstellar medium (ISM) and the formation process of low-mass prestellar cores (André et al. 2010). While molecular clouds were already known to exhibit large-scale filamentary structures for quite some time (e.g. Schneider & Elmegreen 1979; Myers 2009, and references therein), *Herschel* observations now demonstrate that these fila-ments are truly ubiquitous in the cold ISM (e.g. Molinari et al. 2010; Henning et al. 2010; Hill et al. 2011), probably make up a dominant fraction of the dense gas in molecular clouds (e.g. Schisano et al. 2014; Könyves et al. 2015), and present a high degree of universality in their properties (e.g. Arzouma-nian et al. 2011). Therefore, interstellar filaments likely play a central role in the star formation process (e.g. André et al. 2014). A detailed analysis of their radial column density pro-files shows that, at least in the nearby clouds of the Gould Belt, filaments are characterized by a very narrow distribution of in-ner widths W with a typical FWHM value ∼ 0.1 pc (much larger than the ∼ 0.01 pc resolution provided by *Herschel* at the dis-tance ∼ 140 pc of the nearest clouds) and a dispersion of less than a factor of 2 (Arzoumanian et al. 2011; Koch & Rosolowsky 2015). The origin of this common inner width of interstellar fila-ments is not yet well understood. A possible interpretation is that it corresponds to the sonic scale below which interstellar turbu-lence becomes subsonic in diffuse, non-star-forming molecular gas (cf. Padoan et al. 2001; Federrath 2016). Alternatively, this

characteristic inner width of filaments may be set by the dissipation mechanism of magneto-hydrodynamic (MHD) waves (e.g. Hennebelle & André 2013). A possible manifestation of such MHD waves may actually have been found in the form of braided velocity-coherent substructure in the case of the Taurus B211–3 filament (Hacar et al. 2013). Another major result from *Herschel* in nearby clouds is that most (> 75%) low-mass prestellar cores and protostars are found in dense, "supercritical" filaments for which the mass per unit length M_{line} exceeds the critical line mass of nearly isothermal, long cylinders (e.g. Inutsuka & Miyama 1997), $M_{line,crit} = 2 c_s^2/G \sim 16\,M_\odot/$pc, where $c_s \sim 0.2$ km/s is the isothermal sound speed for molecular gas at $T \sim 10$ K (e.g. Könyves et al. 2015). These *Herschel* findings support a scenario for low-mass star formation in two main steps (cf. André et al. 2014): First, large-scale compression of interstellar material in supersonic MHD flows generates a cobweb of ~ 0.1 pc-wide filaments in the ISM; second, the densest filaments fragment into prestellar cores (and subsequently protostars) by gravitational instability above $M_{line,crit}$, while simultaneously growing in mass through accretion of background cloud material.

In addition to the relatively modest filaments found in non star forming and low-mass star forming clouds, where M_{line} rarely exceeds ten times the thermal value of $M_{line,crit}$, significantly denser and more massive filamentary structures have also been observed in the most active giant molecular clouds (GMCs) of the Galaxy, and may be the progenitors of young massive star clusters. The DR21 main filament or "ridge" is probably the most emblematic case of such a massive elongated structure with about $20000\,M_\odot$ inside a 4.5 pc long structure (i.e., $M_{line} \sim 4500\,M_\odot/$pc) (Motte et al. 2007; Schneider et al. 2010; Hennemann et al. 2012). Other well-known ridges include Orion A (Hartmann & Burkert 2007), Vela-C (Hill et al. 2011, 2012), IRDC G035.39–00.33 (Nguyen Luong et al. 2011), and W43-MM1 (Nguyen-Luong et al. 2013; Louvet et al. 2014). These ridges, which exceed the critical line mass of an isothermal filament by up to two orders of magnitude, are believed to be in a state of global collapse, to be fed by very high accretion rates on large scales (Schneider et al. 2010; Peretto et al. 2007, 2013), and to continuously form stars and clusters. The formation of these ridges is not yet well understood but may result from the large-scale collapse of a significant portion of a GMC (Hartmann & Burkert 2007; Schneider et al. 2010).

Whether the low-mass star formation scenario summarized above – or an extension of it – also applies to regions dominated by hyper-massive clumps and ridge-like structures (Motte et al. 2016) is not yet known. In particular, further work is needed to confirm that the inner width of interstellar filaments remains close to ~ 0.1 pc in regions of massive star formation beyond the Gould Belt, where the moderate angular resolution of *Herschel* (HPBW ~ 18–$36''$ at $\lambda = 250$–$500\,\mu$m) is insufficient to resolve this characteristic scale.

At a distance of ~ 1.7 kpc, NGC 6334 is a very active complex of massive star formation (Persi & Tapia 2008; Russeil et al. 2013) with about 150 associated luminous stars of O- to B3-type (Neckel 1978; Bica et al. 2003; Feigelson et al. 2009). At far-infrared and (sub)millimeter wavelengths, the central part of NGC 6334 consists of a 10 pc-long elongated structure including two major high-mass star-forming clumps and a narrow filament (e.g. Sandell 2000; Tigé et al. 2016). The filament is particularly prominent in ground-based (sub)millimeter continuum images where extended emission is effectively filtered (e.g. Muñoz et al. 2007; Matthews et al. 2008). It apparently forms only low-mass stars (Tigé et al. 2016), except perhaps at its end points,

in marked contrast with the high-mass clumps which host several protostellar "massive dense cores" (Sandell 2000; Tigé et al. 2016). The multi-wavelength coverage and high dynamic range of *Herschel* observations from the HOBYS key project (Motte et al. 2010) gave an unprecedented view of the column density and dust temperature structure of NGC 6334 with a resolution limited to $36''$ or 0.3 pc when the $500\,\mu$m band was used (Russeil et al. 2013 and Tigé et al. 2016). The NGC 6334 filament has a line mass approaching $M_{line} \sim 1000\,M_\odot/$pc and features column densities close to or above 10^{23} cm^{-2} over about 10 pc along its length (e.g. Matthews et al. 2008; Zernickel et al. 2013).

Here, we report the results of high-resolution ($8''$) $350\,\mu$m dust continuum mapping observations of the central part of NGC 6334 with the ArTéMiS bolometer camera on the APEX 12-m telescope. The $\sim 8''$ resolution of ArTéMiS at $350\,\mu$m, corresponding to ~ 0.068 pc at the distance of NGC 6334, has allowed us to resolve, for the first time, the transverse size of the main filament in this complex. Section 2 describes the instrument and provides details about the observing run and data reduction. Section 3 presents our mapping results, which are discussed in Section 4.

2. ArTéMiS observations and data reduction

Our $350\,\mu$m observations of NGC 6334 were obtained in July–September 2013 and June 2014 with the ArTéMiS[1] camera on the Atacama Pathfinder Experiment (APEX) telescope located at an altitude of 5100 m at Llano de Chajnantor in Chile. ArTéMiS is a large-format bolometer array camera, built by CEA/Saclay and installed in the Cassegrain cabin of APEX, which will eventually have a total of 4608 pixels observing at $350\,\mu$m and $450\,\mu$m simultaneously (Talvard et al. 2010; Revéret et al. 2014).

ArTéMiS employs the technology successfully developed by CEA for the PACS photometer instrument in the 60–210 μm wavelength regime on the *Herschel* Space Observatory (e.g. Billot et al. 2006). Unlike the LABOCA camera on APEX, the ArTéMiS instrument does not use feedhorns to concentrate the incoming submillimeter radiation, but planar bare arrays of 16×18 silicon bolometer pixels each which act like a CCD camera does in the optical domain. The 2013 and 2014 incarnations of ArTéMiS used for these observations were equipped with a $350\,\mu$m focal plane of four and eight such sub-arrays of 16×18 pixels, respectively. The number of working pixels was about 1050 in 2013 and 1650 in 2014. The instantaneous field of view of the camera was $\sim 2.1' \times 2.4'$ in 2013 and $\sim 4.3' \times 2.4'$ in 2014, and was essentially fully sampled. ArTéMiS features a closed-cycle cryogenic system built around a pulse tube cooler (40 K and 4 K) coupled to a double stage helium sorption cooler (~ 300 mK). During the 2013 and 2014 observing campaigns, the typical hold time of the cryostat at 260 mK between two remote recycling procedures at the telescope was > 48 hours.

A total of 35 individual maps, corresponding to a total telescope time of ~ 13 hr (excluding pointing, focusing, and calibration scans), were obtained with ArTéMiS at $350\,\mu$m toward the NGC 6334 region using a total-power, on-the-fly scanning mode. Each of these maps consisted in a series of scans taken either in Azimuth or at a fixed angle with respect to the Right Ascension axis. The scanning speed ranged from $20''$/sec to $30''$/sec and the cross-scan step between consecutive scans from $3''$ to $10''$.
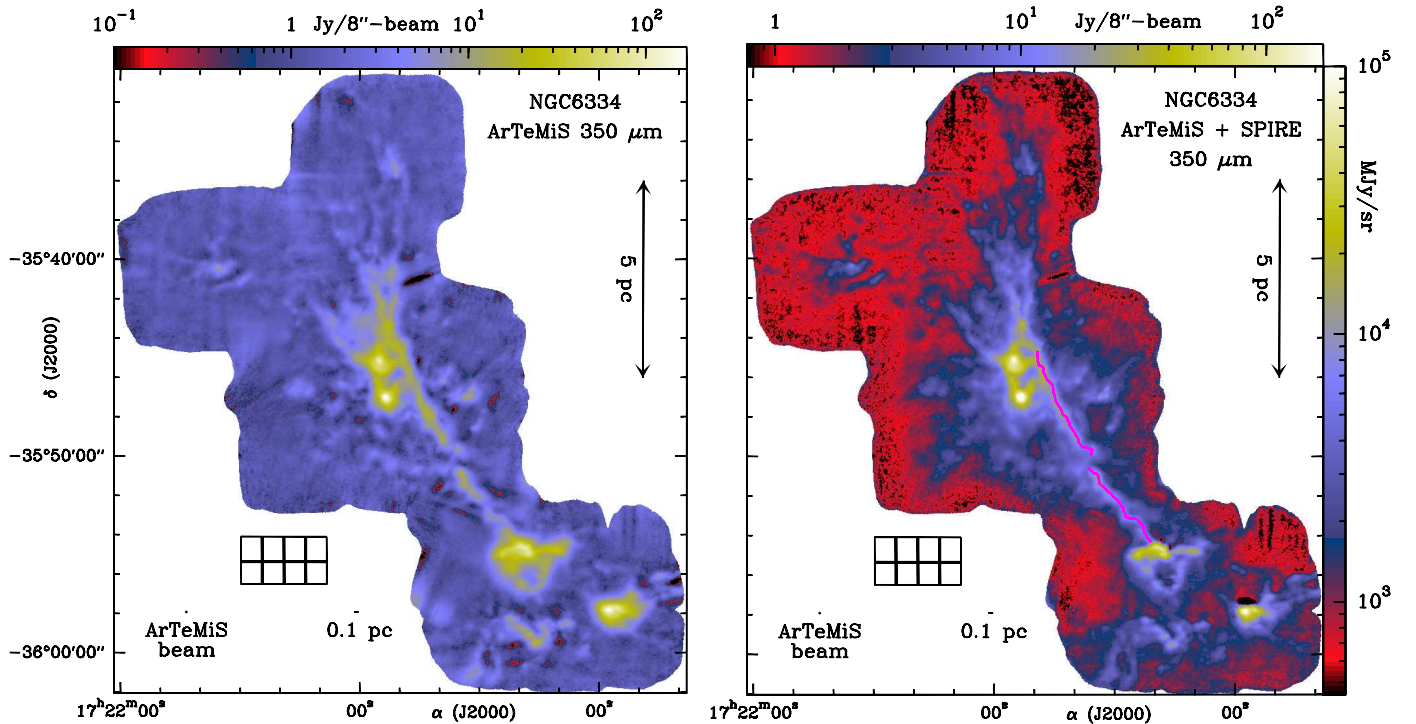

Fig. 1. **(a)** ArTéMiS 350 μm dust continuum mosaic of the central part of the NGC 6334 star-forming complex. The effective half-power beam width (HPBW) resolution is 8″ (or 0.07 pc at $d = 1.7$ kpc), a factor of > 3 higher than the *Herschel*/HOBYS SPIRE 350 μm map (Russeil et al. 2013; Tigé et al. 2016). **(b)** High dynamic range 350 μm dust continuum map of the same field obtained by combining the ArTéMiS high-resolution data shown in the left panel with the *Herschel*/SPIRE 350 μm data providing better sensitivity to large-scale emission. The effective angular resolution is also 8″ (HPBW). The crest of the main filament as traced by the DisPerSE algorithm (Sousbie 2011) is marked by the magenta curve. The footprint of the 4×2 sub-arrays of the ArTéMiS camera indicating the instantaneous field of view on the sky is shown in both panels. (The instantaneous field of view for the data taken in 2013 corresponds to the central 2×2 sub-arrays.)

The sizes of the maps ranged from $3.5' \times 3.5'$ to $11.5' \times 10'$. The atmospheric opacity at zenith was measured using skydips with ArTéMiS and was found to vary between 0.45 and 1.85 at $\lambda = 350\,\mu$m. This is equivalent to an amount of precipitable water vapor (PWV) from ~ 0.25 mm to ~ 0.9 mm with a median value of 0.53 mm. The median elevation of NGC 6334 was $\sim 58°$ corresponding to a median airmass of 1.18.

A dedicated pointing model was derived for ArTéMiS after the first days of commissioning observations in July 2013 and was found to yield good results (3″ overall rms error) throughout the ArTéMiS observing campaign. Absolute calibration was achieved by taking both short 'spiral' scans and longer on-the-fly beam maps of the primary calibrators Mars and Uranus. During the mapping of NGC 6334, regular pointing, focus, and calibration checks were made by observing 'spiral' scans of the nearby secondary calibrators G5.89, G10.47, G10.62, and IRAS 16293. The maximum deviation observed between two consecutive pointing checks was $\sim 3''$. The absolute pointing accuracy is estimated to be $\sim 3''$ and the absolute calibration uncertainty to be $\sim 30\%$.

The median value of the noise equivalent flux density (NEFD) per detector was ~ 600 mJy s$^{1/2}$, with best pixel values at ~ 300 mJy s$^{1/2}$. The pixel separation between detectors on the sky was $\sim 3.9''$, corresponding to Nyquist spacing at 350 μm. As estimated from our maps of Mars, the main beam had a full width at half maximum (FWHM) of $8.0 \pm 0.1''$ and contained $\sim 70\%$ of the power, the rest being distributed in an "error beam" extending up to an angular radius of $\sim 40''$ (see blue solid curve in Fig. 3a in Sect. 3 below for the beam profile).

Online data reduction at the telescope was performed with the BoA software developed for LABOCA (Schuller 2012). Offline data reduction, including baseline subtraction, removal of correlated skynoise and $1/f$ noise, and subtraction of uncorrelated $1/f$ noise was performed with in-house IDL routines, including tailored versions of the Scanamorphos software routines which exploit the redundancy in the mapping raw data, especially data taken with filled arrays. The Scanamorphos algorithm, as developed to process *Herschel* observations, is described in depth in Roussel (2013). To account for the specificities of the observations discussed here, it had to be modified. The destriping step for long scans had to be deactivated, as well as the average drift subtraction in scans entirely filled with sources, and a sophisticated filter had to be applied to subtract the correlated skynoise. This filter involves a comparison between the signal of all sub-arrays at each time, and a protection of compact sources by means of a mask initialized automatically, and checked manually.

3. Mapping results and radial profile analysis

By co-adding the 35 individual ArTéMiS maps of NGC 6334, we obtained the 350 μm mosaic shown in Fig. 1a. The typical rms noise in this mosaic is $\sigma \sim 0.2$ Jy/8″-beam. As usual with total-power ground-based submillimeter continuum observations, the ArTéMiS raw data were affected by a fairly high level of skynoise, strongly correlated over the multiple detectors of the focal plane. Because of the need to subtract this correlated skynoise to produce a meaningful image, the mosaic of Fig. 1a is not sensitive to angular scales larger than the instantaneous
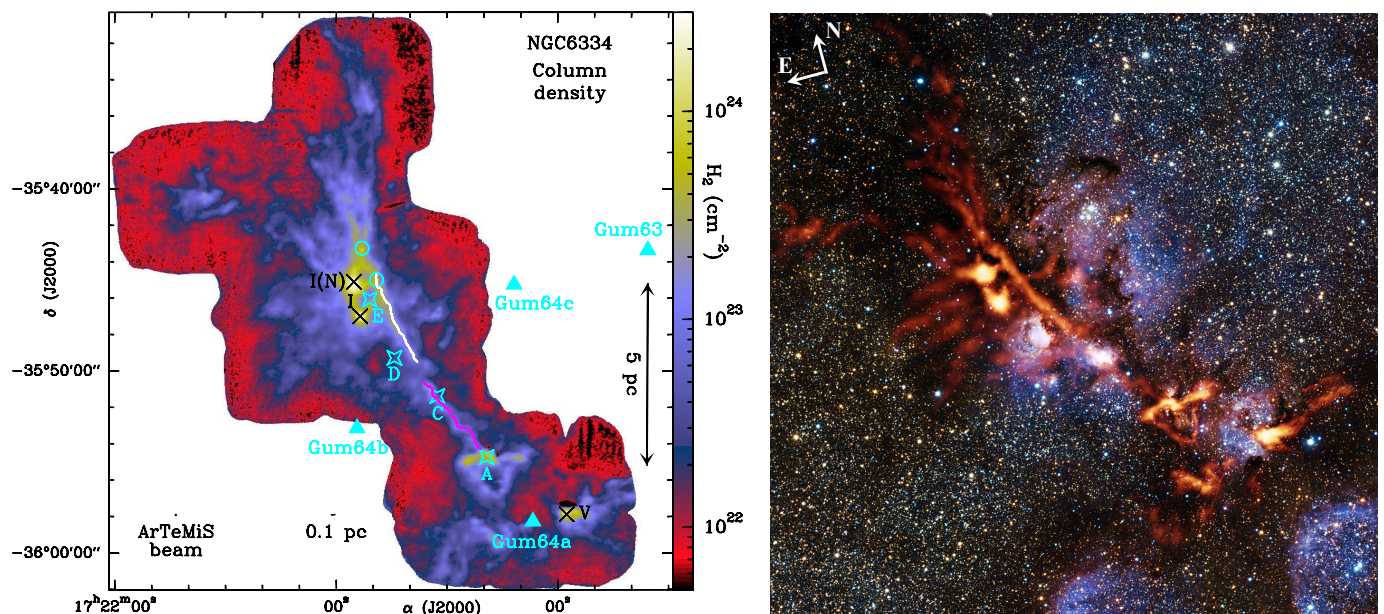
Fig. 2. (a) Approximate H$_2$ column density map of the central part of the NGC 6334 star-forming complex derived from the combined ArTéMiS + SPIRE 350 μm image shown in Fig. 1b, assuming optically thin dust emission at the temperature given by the *Herschel*/HOBYS dust temperature map of Tigé et al. (2016) (see also Russeil et al. 2013). The effective angular resolution is 8″ (HPBW). The crest of the northern part of the NGC 6334 main filament as traced by the DisPerSE algorithm (Sousbie 2011) is marked by the white curve, while the crest of the southern part is shown by the magenta curve. Black crosses and roman numerals (I, V) denote bright far-infrared sources (Kraemer & Jackson 1999). Cyan open circles mark two candidate starless "massive dense cores" from Tigé et al. (2016). Cyan open diamonds and alphabetical letters A–E indicate compact HII regions detected in the 6 cm radio continuum with the VLA (Rodriguez et al. 1982), and cyan filled triangles mark diffuse HII regions traced as diffuse Hα emission nebulosities (Gum 1955). **(b)** ArTéMiS 350 μm image (orange) overlaid on a view of the same region taken at near-infrared wavelengths with the ESO VISTA telescope (see ESO photo release http://www.eso.org/public/images/eso1341a/ – Credit: ArTéMiS team/ESO/J. Emerson/VISTA).

field of view of the camera ∼ 2′. The large-scale background intensity (e.g. zero level) in the image of Fig. 1a is therefore not constrained by the ArTéMiS observations and has been arbitrarily set to a small positive value (corresponding approximately to ∼ 5σ) to facilitate the display using a logarithmic intensity scale. To restore the missing large-scale information, we combined the ArTéMiS data with the SPIRE 350 μm data from the *Herschel* HOBYS key project (Motte et al. 2010; Russeil et al. 2013) employing a technique similar to that used in combining millimeter interferometer observations with single-dish data. In practice, this combination was achieved with the task "immerge" in the Miriad software package (Sault et al. 1995). Immerge combines two datasets in the Fourier domain after determining an optimum calibration factor to align the flux scales of the two input images in a common annulus of the uv plane. Here, a calibration factor of 0.75 had to be applied to the original ArTéMiS image to match the flux scale of the SPIRE 350 μm image over a range of baselines from 0.6 m (the baseline b sensitive to angular scales b/λ ∼ 2′ at 350 μm) to 3.5 m (the diameter of the *Herschel* telescope). The magnitude of this factor is consistent with the absolute calibration uncertainty of ∼ 30% quoted in Sect. 2. The resulting combined 350 μm image of NGC 6334 has an effective resolution of ∼ 8″ (FWHM) and is displayed in Fig. 1b.

To determine the location of the crest of the main filament in NGC 6334, we applied the DisPerSE algorithm (Sousbie 2011) to the combined 350 μm image. The portion of the filament analyzed in some detail below was selected so as to avoid the confusing effects of massive young stars and protostellar "massive dense cores" (MDCs) (cf. Tigé et al. 2016). It nevertheless includes one candidate starless MDC at its northern end (see

Fig. 2a). The corresponding crest is shown as a magenta solid curve in Fig. 1b.

By taking perpendicular cuts at each pixel along the crest, we constructed radial intensity profiles for the main filament. The western part of the resulting median radial intensity profile is displayed in log-log format in Fig. 3a. Since at least in projection there appears to be a gap roughly in the middle of the filament crest (cf. Fig. 1), we also divided the filament into two parts, a northern and a southern segment, shown by the white and the magenta curve in Fig. 2a, respectively. The gap between the two segments may have been created by an HII region visible as an Hα nebulosity in Fig. 2b. Separate radial intensity profiles for the northern and southern segments are shown in Fig. A.1 and Fig. A.2, respectively. Due to the presence of the two massive protostellar clumps NGC 6334 I and I(N) (Sandell 2000, see also Fig. 2a), it is difficult to perform a meaningful radial profile analysis on the eastern side of the northern segment, and the corresponding intensity profile has larger error bars (cf. Fig. A.1a).

Following Arzoumanian et al. (2011) and Palmeirim et al. (2013) we fitted each radial profile $I(r)$ observed as a function of radius r with both a simple Gaussian model:

$$I_G(r) = I_0 \times \exp\left[-4\ln 2 \times \left(r/\overline{\mathrm{FWHM}}\right)^2\right] + I_{Bg}, \qquad (1)$$

and a Plummer-like model function of the form:

$$I_p(r) = \frac{I_0}{\left[1 + (r/R_{\mathrm{flat}})^2\right]^{\frac{p-1}{2}}} + I_{Bg}, \qquad (2)$$

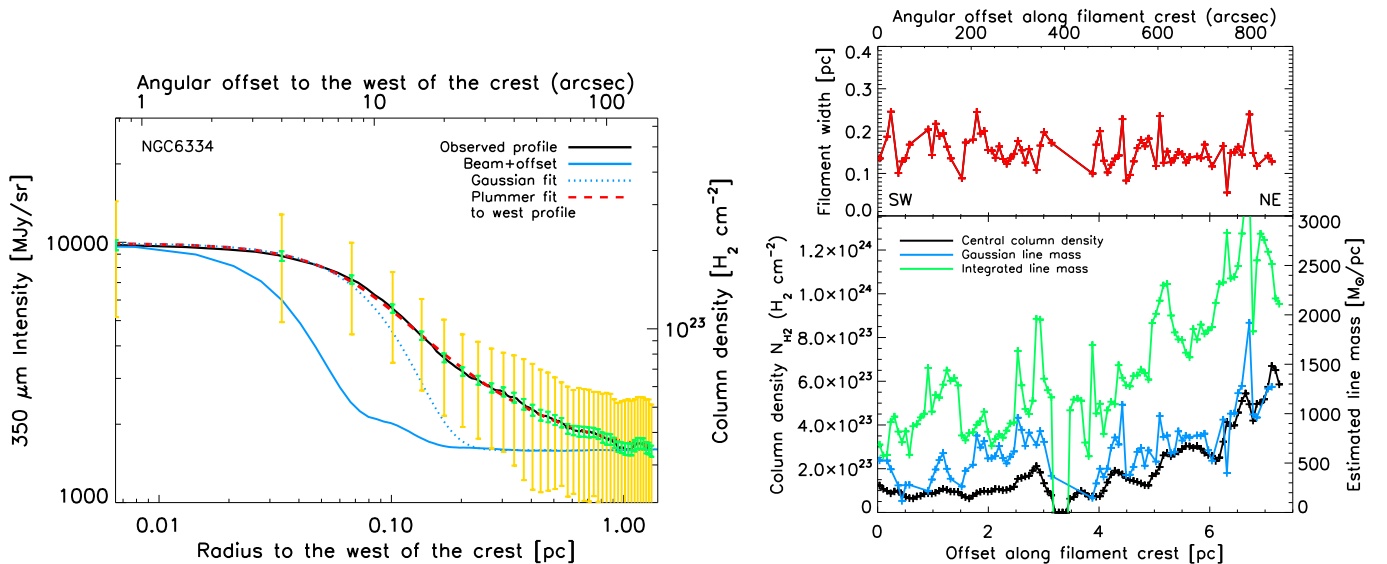**Fig. 3.** **(a)** Median radial intensity profile of the NGC 6334 filament (black solid curve) measured perpendicular to, and on the western side of, the filament crest shown as a magenta curve in Fig. 1b. The yellow error bars visualize the ($\pm 1\sigma$) dispersion of the *distribution* of radial intensity profiles observed along the filament crest, while the smaller green error bars represent the standard deviation of the *mean* intensity profile (the data points and error bars are spaced by half a beam width). The blue solid curve shows the effective beam profile of the ArTéMiS 350 μm data as measured on Mars, on top of a constant level corresponding to the typical background intensity level observed at large radii. The blue dotted curve shows the best-fit Gaussian (+ constant offset) model to the inner part of the observed profile. The red dashed curve shows the best-fit Plummer model convolved with the beam as described in the text. **(b)** *Upper panel:* Deconvolved Gaussian FWHM width of the NGC 6334 filament as a function of position along the filament crest (from south-west to north-east), with one width measurement per independent ArTéMiS beam of 8'' (red crosses). *Lower panel:* Observed column density (black curve and left y-axis), background-subtracted mass per unit length (blue curve and right y-axis) derived from a Gaussian fit (cf. blue dotted curve in **(a)**) to the filament transverse profile, and background-subtracted mass per unit length (green curve and right y-axis) derived from integration of the observed transverse profile (cf. black curve in **(a)**) up to an outer radius of 0.7 pc (or $\sim 80''$) where the background starts to dominate, all plotted as a function of position along the filament crest.

where I_0 is the central peak intensity, $\overline{\text{FWHM}}$ is the physical FWHM width of the Gaussian model, R_{flat} the characteristic radius of the flat inner part of the model profile, $p > 1$ is the power-law index of the underlying density profile (see below), and I_{Bg} is a constant background level. The above functional forms were convolved with the approximately Gaussian beam of the ArTéMiS data (FWHM $\sim$ 8'') prior to comparison with the observed profile. The best-fit Gaussian and Plummer-like models for the median radial intensity profile observed on the western side of the entire filament are shown by the blue dotted and red dashed curves in Fig. 3a, respectively. Note that only the inner part of the radial profile was fitted with a Gaussian model since the observed profile includes an approximately power-law wing which cannot be reproduced by a Gaussian curve (cf. Fig. 3a). In practice, a background level was first estimated as the intensity level observed at the closest point to the filament's crest for which the logarithmic slope of the radial intensity profile d ln I/d ln r became significantly positive. This allowed us to obtain a crude estimate of the width of the profile at half power above the background level, and the observed profile was then fitted with a Gaussian model over twice this initial width estimate. The deconvolved diameter of the best-fit Gaussian model is $\overline{\text{FWHM}}$ = 0.15 $\pm$ 0.02 pc and the diameter of the inner plateau in the best-fit Plummer model is $2 R_{\text{flat}}$ = 0.11 $\pm$ 0.03 pc. The power-law index of the best-fit Plummer model is p = 2.2 $\pm$ 0.3. Assuming optically thin dust emission at 350 μm and using the dust temperature map derived from *Herschel* data at 36.3'' resolution (Russeil et al. 2013; Tigé et al. 2016), we also converted the 350 μm image of Fig. 1b (I_{350}) into an approximate column density image (see Fig. 2a) from the simple relation $N_{H_2} = I_{350}/(B_{350}[T_d]\kappa_{350}\mu_{H_2} m_H)$, where B_{350} is

the Planck function, T_d the dust temperature, κ_{350} the dust opacity at $\lambda = 350 \mu$m, and μ_{H_2} = 2.8 the mean molecular weight. We adopted the same dust opacity law as in our HGBS and HOBYS papers: κ_λ = 0.1 $\times$ (λ/300 μm)$^{-\beta}$ cm^2 per g (of gas + dust) with an emissivity index β = 2 (Hildebrand 1983; Roy et al. 2014). The y-axis shown on the right of Fig. 3a gives an approximate column density scale derived in this way for the median radial profile of the filament assuming a uniform temperature T_d = 20 K, which corresponds to the median dust temperature derived from *Herschel* data along the crest of the filament. We also derived and fitted a median radial column density profile for the filament directly using the column density map (see Fig. A.3 in Appendix A). The results of our radial profile analysis for the whole filament and its two separate segments are summarized in Table 1, which also provides a comparison with similar measurements reported in the recent literature for four other well-documented filaments.

We stress that the presence of cores along the filament has virtually no influence on the results reported in Table 1. First, as already mentioned the portion of the filament selected here contains only one candidate starless MDC at the northern end (cf. Tigé et al. 2016), and the width estimates are unchanged when the immediate vicinity of this object is excluded from the analysis (see also Fig. 3b). Second, low-mass prestellar cores typically contribute only a small fraction ($\lesssim$ 15%) of the mass of dense filaments (e.g. Könyves et al. 2015). Third, we performed the same radial profile analysis on a source-subtracted image generated by *getsources* (Men'shchikov et al. 2012) and obtained very similar results.

One advantage of the Plummer-like functional form in Eq. (2) is that, when applied to a filament column density profile

Table 1. Derived properties of the NGC 6334 filament and comparison with other well-documented filaments

Filament	$\langle M_{\rm line} \rangle$ [a] ($M_\odot$/pc)	$\langle N_{\rm H_2}^0 \rangle$ [b] (cm^{-2})	$N_{\rm H_2}^{\rm bg}$ [c] (cm^{-2})	p [d]	$R_{\rm flat}$ [e] (pc)	Width, W [f] (pc)	Length (pc)	Refs
NGC 6334 north+south (western side)	800–1300	1–2×10^{23}	1.8×10^{22}	2.2 ± 0.3	0.05 ± 0.01	0.15 ± 0.03	> 7	1
NGC 6334 north+south (eastern side)	(900–1300)	$(1$–$2\times10^{23})$	$(2$–$4\times10^{22})$	(1.9 ± 0.4)	(0.05 ± 0.02)	(0.19 ± 0.03)	> 7	1
NGC 6334 north (western side)	1600	2.5×10^{23}	2.1×10^{22}	2.4 ± 0.3	0.06 ± 0.02	0.15 ± 0.03	> 3.5	1
NGC 6334 north[g] (eastern side)	(800–1600)	$(1.5$–$2.5\times10^{23})$	(1.1×10^{23})	–	–	(0.20 ± 0.03)	> 3.5	1
NGC 6334 south (western side)	500–600	0.7–1×10^{23}	1.2×10^{22}	(2.3 ± 0.3)	(0.07 ± 0.02)	0.16 ± 0.04	~ 3	1
NGC 6334 south (eastern side)	700–2000	0.9–1×10^{23}	1.2×10^{22}	1.8 ± 0.3	0.09 ± 0.02	0.16 ± 0.04	~ 3	1
Vela C[h]	320–400	8.6×10^{22}	3.6×10^{21}	2.7 ± 0.2	0.05 ± 0.02	0.12 ± 0.02	4	2
Serpens South	290	6.4×10^{22}	3.7×10^{21}	2.0 ± 0.3	0.03 ± 0.01	0.10 ± 0.05	2	2, 3
Taurus B211/B213	50	1.5×10^{22}	0.7×10^{21}	2.0 ± 0.3	0.03 ± 0.02	0.09 ± 0.02	> 5	4
Musca	20	4.2×10^{21}	0.8×10^{21}	2.2 ± 0.3	0.08	0.14 ± 0.03	10	5, 6

Notes. Values given in parentheses are more uncertain due to, e.g., large error bars in the corresponding filament profiles, and should be understood as being only indicative.
[a] Average mass per unit length of the equivalent cylindrical filament derived from one-sided integration of the observed radial column density profile after background subtraction. The actual mass per unit length of each filament segment corresponds to the mean of the eastern-side and western-side values (not explicitly given here). The outer radius of integration was 0.7 pc on the western side, 0.3 pc on the eastern side of the northern segment, and 1.4 pc on the eastern side of the southern segment, respectively, corresponding to the radius where the background starts to dominate (see Figs. A.1–A.3).
[b] Average value of the central column density derived along the filament crest after background subtraction. Typical uncertainties are a factor ~ 1.5–2 for values $< 10^{23}$cm^{-2} and a factor ~ 2–3 for values $> 10^{23}$cm^{-2}, dominated by uncertainties in the dust opacity and in the distribution of dust temperature along the line of sight (Roy et al. 2014).
[c] Background column density. This is estimated as the column density observed at the closest point to the filament's crest for which the logarithmic slope of the radial column density profile d ln $N_{\rm H_2}$/d ln r becomes positive.
[d] Power-law index of the best-fit Plummer model [see Eq. (2)].
[e] Radius of the flat inner plateau in the best-fit Plummer model [see Eq. (2)].
[f] Deconvolved FWHM width from a Gaussian fit to the inner part of the filament profile.
[g] The eastern side of the radial column density profile of the northern filament is poorly constrained due to confusion with the two massive protostellar clumps NGC 6334 I and I(N) (cf. Fig. 2a); no meaningful Plummer fit is possible.
[h] According to Minier et al. (2013), the Vela C filament is not a simple linear structure or "ridge", but is part of a more complex ring-like structure at least partly shaped by ionization associated with the RCW 36 HII region.

References. (1) this paper; (2) Hill et al. (2012); (3) Könyves et al. (2015); (4) Palmeirim et al. (2013); (5) Cox et al. (2016); (6) Kainulainen et al. (2016).

(I_0 becoming $N_{\rm H_2,0}$, the central column density), it directly informs about the underlying volume density profile, which takes a similar form, $n_p(r) = \frac{n_{\rm H_2,0}}{\left[1+(r/R_{\rm flat})^2\right]^{p/2}}$, where $n_{\rm H_2,0}$ is the central volume density of the filament. The latter is related to the projected central column density $N_{\rm H_2,0}$ by the simple relation, $n_{\rm H_2,0} = N_{\rm H_2,0}/(A_p\, R_{\rm flat})$, where $A_p = \frac{1}{\cos i} \times B\left(\frac{1}{2}, \frac{p-1}{2}\right)$ is a constant factor taking into account the filament's inclination angle to the plane of the sky, and B is the Euler beta function (cf. Palmeirim et al. 2013). Here, assuming $i = 0°$, we estimate the mean central density to be $n_{\rm H_2,0} \sim 2.2\times10^5$ cm^{-3}, $\sim 5\times10^5$ cm^{-3}, and $\sim 1.5\times10^5$ cm^{-3} in the entire filament, the northern segment, and the southern segment, respectively.

4. Discussion and conclusions

Our ArTéMiS mapping study confirms that the main filament in NGC 6334 is a very dense, massive linear structure with $M_{\rm line}$ ranging from $\sim 500\, M_\odot$/pc to $\sim 2000\, M_\odot$/pc over nearly 10 pc, and demonstrates for the first time that its inner width remains as narrow as $W \sim 0.15 \pm 0.04$ pc all along the filament length (see Fig. 3b), within a factor of < 2 of the characteristic 0.1 pc value

found by Arzoumanian et al. (2011) for lower-density nearby filaments in the Gould Belt.

While the NGC 6334 filament is highly supercritical, and of the same order of magnitude in line mass as high-mass star-forming ridges such as DR21 (Schneider et al. 2010; Hennemann et al. 2012), it is remarkably simple and apparently consists of only a single, narrow linear structure. In contrast, a massive ridge is typically resolved into a closely packed network of sub-filaments and "massive dense cores" (MDCs) (Motte et al. 2016). This is at variance with the NGC 6334 filament which exhibits a surprisingly low level of fragmentation. The maximum relative column density fluctuations observed along its long axis (cf. black curve in Fig. 3b) are only marginally nonlinear ($\delta N_{\rm H_2}/\langle N_{\rm H_2} \rangle \approx 1$), while for instance most of the supercritical low-mass filaments analyzed by Roy et al. (2015) have stronger fluctuations (with $\delta N_{\rm H_2}/\langle N_{\rm H_2} \rangle$ up to ~ 2–5). Most importantly, the NGC 6334 filament harbors no MDC, except perhaps at its two extremities (Tigé et al. 2016, see Fig. 2a). It is therefore unclear whether the filament will form high-mass stars or not. On the one hand, the lack of MDCs suggests that the filament may not form any massive stars in the near future. On the other hand, the presence of a compact HII region (radio source

C from Rodriguez et al. 1982) at the north-east end of the southern part of the filament, near the gap between the two filament segments (see Fig. 2a), suggests that it may have already formed massive stars in the past. Based on observations in the $HCO^+(3-2)$ and $H^{13}CO^+(1-0)$ lines with APEX and MOPRA, Zernickel et al. (2013) showed that the filament is coherent in velocity and found a velocity gradient of $\sim 2\,km\,s^{-1}/pc$ from both ends of the filament toward its center. They proposed that the whole filament is in a state of global collapse along its long axis toward its center (estimated to be close to the gap between the two segments in Fig. 2a). This proposal is qualitatively consistent with the identification of candidate MDCs at the two ends of the filament (Tigé et al. 2016), and with the theoretical expectation that the longitudinal collapse of a finite filament is end-dominated due to maximal gravitational acceleration at the edges (e.g. Burkert & Hartmann 2004; Clarke & Whitworth 2015). It is difficult, however, to explain the presence of HII regions – significantly more evolved than MDCs – near the central gap in this picture, unless these HII regions did not form in the filament but in the vicinity and disrupted the central part of the filament.

The low level of fragmentation poses a challenge to theoretical models since supercritical filaments are supposed to contract radially and fragment along their length in only about one free-fall time or ~ 4.5–8×10^4 yr in the present case (e.g. Inutsuka & Miyama 1997). One possibility is that the NGC 6334 filament is observed at a very early stage after its formation by large-scale compression. Another possibility is that the filament is "dynamically" supported against rapid radial contraction and longitudinal fragmentation by accretion-driven MHD waves (cf. Hennebelle & André 2013). The average one-dimensional velocity dispersion σ_{1D} estimated from the $40''$ resolution $N_2H^+(1-0)$ observations of the MALT90 survey with the MOPRA telescope (Jackson et al. 2013) is $\sim 1.1\,km/s$ in the northern part of the filament and $\sim 0.7\,km/s$ in the southern segment. Compared to the sound speed $c_s \sim 0.3\,km/s$ given an estimated gas temperature $T \sim 20$–$25\,K$, this velocity dispersion is supersonic by a factor ~ 2–4, implying that there may be significant velocity substructure (such as the presence of several sonic velocity components – cf. Hacar et al. 2013) in the filament. Ignoring any static magnetic field, the virial mass per unit length, $M_{line,vir} = 2\,\sigma_{1D}^2/G$ (cf. Fiege & Pudritz 2000), is thus $\sim 560\,M_\odot/pc$ and $\sim 220\,M_\odot/pc$ in the northern and southern segments, respectively, which is consistent with the filament being within a factor of ~ 2 of virial balance. A static magnetic field can easily modify $M_{line,vir}$ by a factor of ~ 2 (cf. Fiege & Pudritz 2000), and a significant static field component perpendicular to the long axis of the filament would help to resist collapse and fragmentation along the filament. Higher-resolution observations in molecular line tracers of dense gas would be needed to investigate whether the NGC 6334 filament contains a bundle of intertwined velocity-coherent fibers similar to the fibers identified by Hacar et al. (2013) in the low-mass B211–3 filament in Taurus. The detection of such braid-like velocity substructure may provide indirect evidence of the presence of internal MHD waves.

In any case, and regardless of whether the NGC 6334 filament will form massive stars or not, our ArTéMiS result that the filament inner width is within a factor of 2 of 0.1 pc has interesting implications. Our NGC 6334 study is clearly insufficient to prove that interstellar filaments have a truly universal inner width, but it shows that the finding obtained with *Herschel* in nearby clouds is not limited to filaments in low-mass star forming regions. It is quite remarkable that the NGC 6334 filament has almost the same inner width as the faint subcritical filaments in Polaris (cf. Men'shchikov et al. 2010; Arzoumanian

et al. 2011), the marginally supercritical filaments in Musca and Taurus (Cox et al. 2016; Palmeirim et al. 2013), or the lower-mass supercritical filaments in Serpens South and Vela C (Hill et al. 2012), despite being three orders of magnitude, two orders of magnitude, and at least a factor of ~ 3 denser and more massive than these filaments, respectively (see Table 1). While not all of these filaments may have necessarily formed in the same way, this suggests that a common physical mechanism is responsible for setting the filament width at the formation stage and that the subsequent evolution of dense filaments – through, e.g., accretion of background cloud material (cf. Heitsch 2013; Hennebelle & André 2013) – is such that the inner width remains at least approximately conserved with time. A promising mechanism for creating dense filaments, which may be quite generic especially in massive star-forming complexes, is based on multiple episodes of large-scale supersonic compression due to interaction of expanding bubbles (Inutsuka et al. 2015). With about 7 bubble-like HII regions per square degree (Russeil et al. 2013, see also Fig. 2), there is ample opportunity for this mechanism to operate in NGC 6334. More specifically, at least in projection, the NGC 6334 filament appears to be part of an arc-like structure centered on the HII region Gum 63 (see Fig. 2a), suggesting the filament may partly result from the expansion of the associated bubble. Interestingly, the background column density is one order of magnitude higher for the NGC 6334 filament than for the other filaments of Table 1, which is suggestive of a significantly stronger compression. Further observational studies will be needed to investigate the structure and environment of a larger number of filaments in massive star forming regions, and will determine whether the characteristics of the NGC 6334 filament are generic or not. More theoretical work is also needed to better understand the physics controlling the width of interstellar filaments.

References

André, P., Di Francesco, J., Ward-Thompson, D., et al. 2014, in Protostars and Planets VI, ed. H. Beuther et al., 27
André, P., Men'shchikov, A., Bontemps, S., et al. 2010, A&A, 518, L102
Arzoumanian, D., André, P., Didelon, P., et al. 2011, A&A, 529, L6
Bica, E., Dutra, C. M., Soares, J., & Barbuy, B. 2003, A&A, 404, 223
Billot, N., Agnèse, P., Auguères, J.-L., et al. 2006, in Society of Photo-Optical Instrumentation Engineers (SPIE) Conference Series, Vol. 6265, Society of Photo-Optical Instrumentation Engineers (SPIE) Conference Series, 62650D
Burkert, A. & Hartmann, L. 2004, ApJ, 616, 288
Clarke, S. D. & Whitworth, A. P. 2015, MNRAS, 449, 1819
Cox, N., Arzoumanian, D., André, P., et al. 2016, A&A, in press
Federrath, C. 2016, MNRAS, 457, 375
Feigelson, E. D., Martin, A. L., McNeill, C. J., Broos, P. S., & Garmire, G. P. 2009, AJ, 138, 227
Fiege, J. D. & Pudritz, R. E. 2000, MNRAS, 311, 85
Gum, C. S. 1955, MmRAS, 67, 155
Hacar, A., Tafalla, M., Kauffmann, J., & Kovács, A. 2013, A&A, 554, A55
Hartmann, L. & Burkert, A. 2007, ApJ, 654, 988
Heitsch, F. 2013, ApJ, 769, 115
Hennebelle, P. & André, P. 2013, A&A, 560, A68
Hennemann, M., Motte, F., Schneider, N., et al. 2012, A&A, 543, L3
Henning, T., Linz, H., Krause, O., et al. 2010, A&A, 518, L95

Hildebrand, R. H. 1983, QJRAS, 24, 267
Hill, T., André, P., Arzoumanian, D., et al. 2012, A&A, 548, L6
Hill, T., Motte, F., Didelon, P., et al. 2011, A&A, 533, A94
Inutsuka, S.-i., Inoue, T., Iwasaki, K., & Hosokawa, T. 2015, A&A, 580, A49
Inutsuka, S.-I. & Miyama, S. M. 1997, ApJ, 480, 681
Jackson, J. M., Rathborne, J. M., Foster, J. B., et al. 2013, PASA, 30, e057
Kainulainen, J., Hacar, A., Alves, J., et al. 2016, A&A, 586, A27
Koch, E. W. & Rosolowsky, E. W. 2015, MNRAS, 452, 3435
Könyves, V., André, P., Men'shchikov, A., et al. 2015, A&A, 584, A91
Kraemer, K. E. & Jackson, J. M. 1999, ApJS, 124, 439
Louvet, F., Motte, F., Hennebelle, P., et al. 2014, A&A, 570, A15
Matthews, H. E., McCutcheon, W. H., Kirk, H., White, G. J., & Cohen, M. 2008, AJ, 136, 2083
McKee, C. F. & Ostriker, E. C. 2007, ARA&A, 45, 565
Men'shchikov, A., André, P., Didelon, P., et al. 2010, A&A, 518, L103
Men'shchikov, A., André, P., Didelon, P., et al. 2012, A&A, 542, A81
Minier, V., Tremblin, P., Hill, T., et al. 2013, A&A, 550, A50
Molinari, S., Swinyard, B., Bally, J., et al. 2010, A&A, 518, L100
Motte, F., Bontemps, S., Schilke, P., et al. 2007, A&A, 476, 1243
Motte, F., Bontemps, S., & Tigé, J. 2016, in IAU Symposium, Vol. 315, From Interstellar Clouds to Star-Forming Galaxies: Universal Processes?, ed. P. Jablonka, P. André, & F. van der Tak, in press
Motte, F., Zavagno, A., Bontemps, S., et al. 2010, A&A, 518, L77
Muñoz, D. J., Mardones, D., Garay, G., et al. 2007, ApJ, 668, 906
Myers, P. C. 2009, ApJ, 700, 1609
Neckel, T. 1978, A&A, 69, 51
Nguyen-Luong, Q., Motte, F., Carlhoff, P., et al. 2013, ApJ, 775, 88
Nguyen Luong, Q., Motte, F., Schuller, F., et al. 2011, A&A, 529, A41
Padoan, P., Juvela, M., Goodman, A. A., & Nordlund, Å. 2001, ApJ, 553, 227
Palmeirim, P., André, P., Kirk, J., et al. 2013, A&A, 550, A38
Peretto, N., Fuller, G. A., Duarte-Cabral, A., et al. 2013, A&A, 555, A112
Peretto, N., Hennebelle, P., & André, P. 2007, A&A, 464, 983
Persi, P. & Tapia, M. 2008, Star Formation in NGC 6334, ed. B. Reipurth, 456
Revéret, V., André, P., Le Pennec, J., et al. 2014, in Society of Photo-Optical Instrumentation Engineers (SPIE) Conference Series, Vol. 9153, Society of Photo-Optical Instrumentation Engineers (SPIE) Conference Series, 915305
Rodriguez, L. F., Canto, J., & Moran, J. M. 1982, ApJ, 255, 103
Roussel, H. 2013, PASP, 125, 1126
Roy, A., André, P., Arzoumanian, D., et al. 2015, A&A, 584, A111
Roy, A., André, P., Palmeirim, P., et al. 2014, A&A, 562, A138
Russeil, D., Schneider, N., Anderson, L. D., et al. 2013, A&A, 554, A42
Sandell, G. 2000, A&A, 358, 242
Sault, R. J., Teuben, P. J., & Wright, M. C. H. 1995, in Astronomical Society of the Pacific Conference Series, Vol. 77, Astronomical Data Analysis Software and Systems IV, ed. R. A. Shaw, H. E. Payne, & J. J. E. Hayes, 433
Schisano, E., Rygl, K. L. J., Molinari, S., et al. 2014, ApJ, 791, 27
Schneider, N., Csengeri, T., Bontemps, S., et al. 2010, A&A, 520, A49
Schneider, S. & Elmegreen, B. G. 1979, ApJs, 41, 87
Schuller, F. 2012, in Society of Photo-Optical Instrumentation Engineers (SPIE) Conference Series, Vol. 8452, Society of Photo-Optical Instrumentation Engineers (SPIE) Conference Series, 84521T
Sousbie, T. 2011, MNRAS, 414, 350
Talvard, M., André, P., Le-Pennec, Y., et al. 2010, in Society of Photo-Optical Instrumentation Engineers (SPIE) Conference Series, Vol. 7741, Society of Photo-Optical Instrumentation Engineers (SPIE) Conference Series, 77410D
Tigé, J., Motte, F., Russeil, D., et al. 2016, to be submitted to A&A
Zernickel, A., Schilke, P., & Smith, R. J. 2013, A&A, 554, L2

[1] Laboratoire AIM, CEA/DRF–CNRS–Université Paris Diderot, IRFU/Service d'Astrophysique, C.E. Saclay, Orme des Merisiers, 91191 Gif-sur-Yvette, France
e-mail: `pandre@cea.fr`
[2] Aix Marseille Université, CNRS, LAM (Lab. d'Astrophysique de Marseille), UMR 7326, 13388 Marseille, France
[3] Institut d'Astrophysique de Paris, Sorbonne Universités, UPMC Univ. Paris 06, CNRS, UMR 7095, 75014 Paris, France
[4] European Southern Observatory, Karl Schwarzschild Str. 2, 85748 Garching bei Munchen, Germany
[5] Univ. Bordeaux, LAB, UMR 5804, 33270, Floirac, France
[6] I. Physik. Institut, University of Cologne, 50937 Köln, Germany
[7] School of Physics & Astronomy, Cardiff University, The Parade, Cardiff CF24 3AA, UK
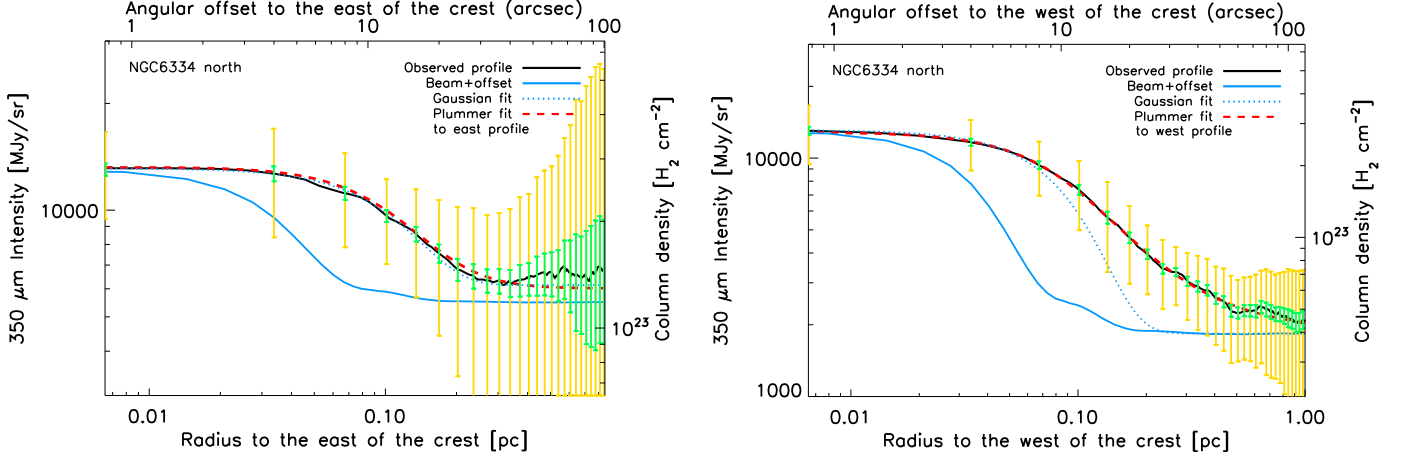[8] INAF-Osservatorio di Radioastronomia, Via P. Gobetti 101, 40129 Bologna, Italy

Appendix A: Additional radial profiles

Fig. A.1. **(a)** Median radial intensity profile of the northern part of the NGC 6334 filament (black solid curve) measured in the combined ArTéMiS + SPIRE 350 μm image (Fig. 1b) perpendicular to, and on the eastern side of, the filament crest shown as a white curve in Fig. 2a. The yellow and green error bars are as in Fig. 3a. The blue solid curve shows the effective beam profile of the ArTéMiS 350 μm data as measured on Mars, on top of a constant level corresponding to the typical background intensity level observed at large radii. The blue dotted curve shows the best-fit Gaussian (+ constant offset) model to the inner part of the observed profile. The red dashed curve shows the best-fit Plummer model convolved with the beam [cf. Sect. 3 and Eq. (2)]. **(b)** Same as in **(a)** but for the median radial intensity profile of the northern part of the filament measured on the western side of the filament crest shown as a white curve in Fig. 2a.
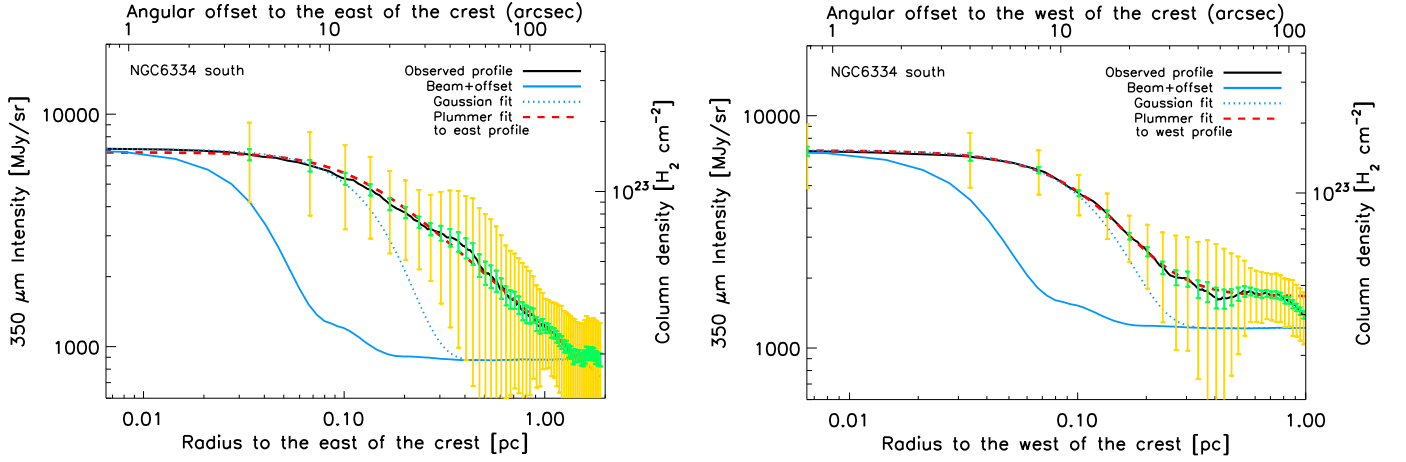

Fig. A.2. **(a)** Median radial intensity profile of the southern part of the NGC 6334 filament (black solid curve) measured in the combined ArTéMiS + SPIRE 350 μm image (Fig. 1b) perpendicular to, and on the eastern side of, the filament crest shown as a magenta curve in Fig. 2a. The yellow and green error bars are as in Fig. 3a. The blue solid curve shows the effective beam profile of the ArTéMiS 350 μm data as measured on Mars, on top of a constant level corresponding to the typical background intensity level observed at large radii. The blue dotted curve shows the best-fit Gaussian (+ constant offset) model to the inner part of the observed profile. The red dashed curve shows the best-fit Plummer model convolved with the beam [cf. Sect. 3 and Eq. (2)]. **(b)** Same as in **(a)** but for the median radial intensity profile of the southern part of the filament measured on the western side of the filament crest shown as a magenta curve in Fig. 2a.
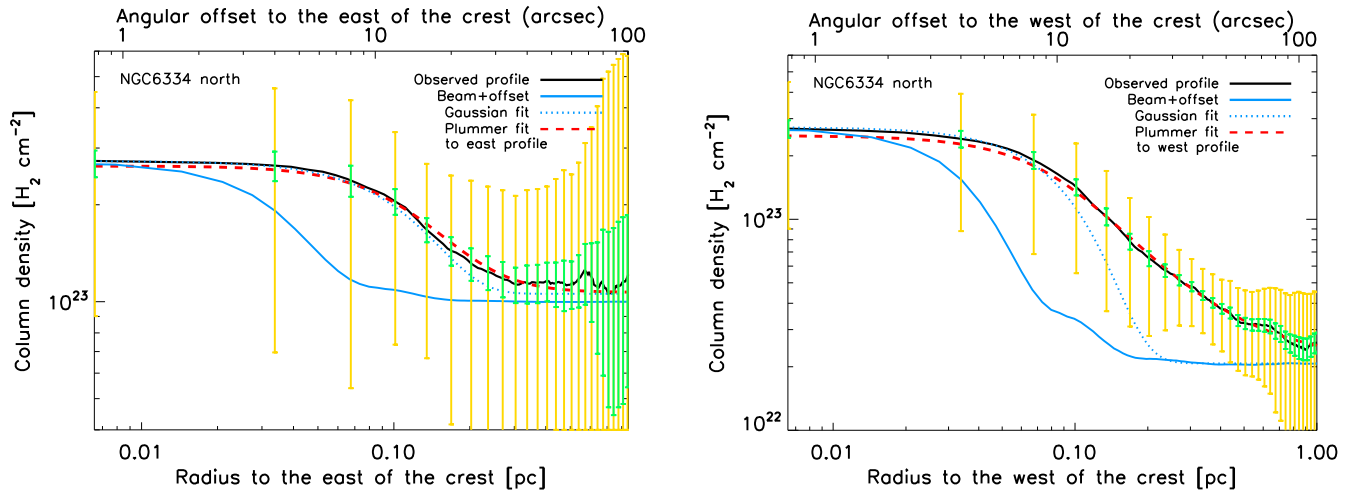
Fig. A.3. **(a)** Same as Fig. A.1a but for the median radial column density profile measured on the eastern side of the northern part of the NGC 6334 filament in the approximate column density map shown in Fig. 2a. **(b)** Same as Fig. A.1b but for the median radial column density profile measured on the western side of the northern part of the filament in the column density map shown in Fig. 2a.